A stabilized meshless method for time-dependent convection-dominated flow problems

Fayssal Benkhaldoun[a], A. Halassi[b,*], Driss Ouazar[c], Mohammed Seaid[d], Ahmed Taik[e]

[a] *Université Paris 13, Sorbonne Paris Cité, CNRS UMR 7539, Laboratoire Analyse, Géométrie, Applications, 99, Avenue Jean-Baptiste Clément, 93430 Villetaneuse, France*
[b] *Université des Comores, Faculté des Sciences et Techniques, Département de Mathématiques, Rue de la Corniche - B.P 2585, Moroni, Comores*
[c] *École nationale supérieure des mines de Rabat, Avenue Hadj Ahmed Cherkaoui - B.P 753, Agdal Rabat, Maroc*
[d] *School of Engineering and Computing Sciences, University of Durham, South Road, DH1 3LE, UK*
[e] *Université Hassan II de Casablanca, Faculté des Sciences et Techniques, Département de Mathématiques, Laboratoire des Mathématiques et Applications, B.P 146 Mohammedia 20650, Maroc*

Abstract

Meshless methods for convection-dominated flow problems have the potential to reduce the computational effort required for a given order of solution accuracy compared to mesh-based methods. The state of the art in this field is more advanced for elliptic partial differential equations than for time-dependent convection–diffusion problems. In this paper, we introduce a new meshless method that it based on combining the modified method of characteristics with the radial basis functions during the solution reconstruction. The method belongs to a class of fractional time-stepping schemes in which a predictor stage is used for the discretization of convection terms and a corrector stage is used for the treatment of diffusion terms. Special attention is given to the application of this method to solve convection-dominated flow problems in two-dimensional domains. Numerical results are shown for several test examples including the incompressible Navier–Stokes equations and the computed results support our expectations for a stable and highly accurate meshless method.

Keywords: Meshless method; Radial basis functions; Modified method of characteristics; Convection-dominated flows; Incompressible Navier–Stokes equations

* Corresponding author.
E-mail address: halassi.abdoul@gmail.com (A. Halassi).

1. Introduction

Convection–diffusion equations have been widely used to model many applications in physical and engineering areas such as weather prediction, ocean circulation, petroleum reservoir etc. The common characteristic in these applications is convective terms are distinctly more important than the diffusive terms; particularly when the Peclet number reaches high values. It is also well-established that these convective terms are a source of computational difficulties and oscillations. On the other hand steep fronts, shocks and boundary layers are among the difficulties that most of numerical methods fail to resolve accurately, see for instance [20]. It is well known that the mesh-based methods use fixed grids and incorporate some upstream weighting in their formulations to stabilize the schemes. These mesh-based methods include the Petrov–Galerkin methods, the streamline diffusion methods and also many other methods such as the high resolution methods from computational fluid dynamics, in particular, the Godunov methods and the essentially non-oscillatory methods, see [8,28] among others. The main shortcoming of these methods lies on the fact that the accuracy of these methods is affected by the quality of the meshes, stabilization techniques and solution of Riemann problems, which hinders their applications to solving real problems with irregular domains and complex Riemann problems.

Recently, significant developments in meshless methods for solving linear as well as nonlinear partial differential equations have been achieved. For instance, the meshless local Petrov–Galerkin and local boundary integral equations methods were investigated in [1,2]. These methods basically transformed the original problem into a local weak formulation and the shape functions were constructed from using the moving least-squares approximation to interpolate the solution variables. The meshless radial basis functions (RBF) have been subject to several studies and their applications to solve partial differential equations have also been covered in the literature. The RBF approximations, particularly the multiquadric basis functions, were first devised for scattered geographical data interpolation in [31,19]. In the interpolation framework, a review on the application of RBF methods for scattered data can be found in [15]. Theoretical results for RBF methods have also been presented in [5,21] among others. These results include solvability, convergence and stability of the RBF interpolation in a general concept. Application of the RBF methods to steady and time-dependent partial differential equations has also been investigated, see for example [13,16]. Recent local formulations of RBF methods have been achieved during this last years [3,26,25,30,24] and some of these local RBF methods have been used to solve hyperbolic systems of conservation laws such as Euler system of gas dynamics and shallow water equations in [27,32,17,7,23]. However, for practical applications in hyperbolic systems, these methods may become computationally demanding due to Riemann solvers in their implementations.

In the current study we propose a stabilized meshless method for convection-dominated flow problems which is simple, accurate and Riemann solver free. This is achieved by combining the Modified Method of Characteristics (MMC) with a class of local radial basis functions. Because of the hyperbolic nature of advective transport in the considered equations, the MMC has been successfully applied to solve convection-dominated flow problems. The MMC carries out the temporal discretization by following the movement of particles along the characteristic curves of the governing equations, see for example [9,29]. Because the solution of advective part is much smoother along the characteristics than they are in the time direction, MMC eliminates the stability restrictions on the Courant number and generates accurate solutions even if large time steps are used in the computations. The idea of developing stable meshless methods to integrate partial differential equations has a long tradition for elliptic class of these equation. This field of research is very active for elliptic equations, where a vast number of numerical schemes have been designed based on global as well local RBF techniques. All of these meshless methods are easy to formulate and to implement. However, their direct application to transient partial differential equations of hyperbolic type results in instabilities, presence of nonphysical oscillations and poor resolution of shocks. The main focus of our work is the development of a truly meshless RBF method to numerically solve the convection-dominated diffusion problems. The key idea in the current approach is a predictor–corrector solver for which the MMC is used in the predictor stage whereas the corrector stage uses the RBF method. The results using the proposed meshless method are presented for three test problems. To the best of our knowledge, solving convection-dominated flow problems using these numerical tools is reported for the first time.

This paper is organized as follows. In Section 2 we present the stabilized meshless method for time-dependent convection–diffusion problems. This section includes both the first fractional step used in the predictor stage to resolve the convection terms and the second fractional step used in the corrector stage for the diffusion terms. Implementation of modified method of characteristics is also covered in this section. Numerical results and examples are presented in

Section 3. We present numerical results for linear convection–diffusion equations and incompressible Navier–Stokes problems. Section 4 contains concluding remarks.

2. A stabilized meshless method

We consider the two-dimensional convection–diffusion flow problem,

$$\begin{aligned} \frac{\partial u}{\partial t} + \mathbf{v}(t,\mathbf{x})\cdot\nabla u - \nu\Delta u &= 0, \quad (t,\mathbf{x}) \in (0,T)\times\Omega, \\ u(0,\mathbf{x}) &= u_0(\mathbf{x}), \quad \mathbf{x}\in\Omega, \end{aligned} \tag{1}$$

where $\mathbf{x} = (x,y)^T$, Ω is a spatial bounded subdomain in $\mathbb{R}^2$ and $[0,T]$ is a time interval. Here $u(t,\mathbf{x})$ denotes the concentration of some species, $\mathbf{v}(t,\mathbf{x}) = (v_1(t,\mathbf{x}), v_2(t,\mathbf{x}))^T$ the velocity field, ν is the diffusion (viscosity) coefficient, and $u_0(\mathbf{x})$ is a given initial function. We assume that appropriate boundary conditions are given in such a way the problem is well defined and has a unique solution. In practice, these conditions are problem dependent and their discussion is postponed for Section 3 where numerical examples will be presented.

The convection–diffusion equation in (1) can also be reformulated in a transport form as

$$\begin{aligned} \frac{Du}{Dt} - \nu\Delta u &= 0, \quad (t,\mathbf{x}) \in (0,T)\times\Omega, \\ u(0,\mathbf{x}) &= u_0(\mathbf{x}), \quad \mathbf{x}\in\Omega, \end{aligned} \tag{2}$$

where the material derivative is defined as

$$\frac{Du}{Dt} = \frac{\partial u}{\partial t} + \mathbf{v}(t,\mathbf{x})\cdot\nabla u. \tag{3}$$

Note that $\frac{Du}{Dt}$ measures the rate of change of the function u following the trajectories of the flow particles. In the current study we also consider the modified method of characteristics (MMC) in our meshless method. The key idea behind the MMC is to impose a regular collocation at the new time level, and to backtrack the flow trajectories to the previous time level. At the old time level, the quantities that are needed are evaluated by interpolation from their known values on a regular collocation.

To formulate our meshless method with more details, we divide the time interval $[0,T]$ into N subintervals $[t_n, t_{n+1}]$ of length Δt such that $t_n = n\Delta t$ $(n = 1,2,\ldots)$ with $T = N\Delta t$, and we assume without loss of generality, a uniform collocation points covering the computational domain Ω as shown in Fig. 1. We use the notations $u^n(\mathbf{x}) = u(t_n,\mathbf{x})$, $u_i(t) = u(t,\mathbf{x}_i)$ and $u_i^n = u(t_n,\mathbf{x}_i)$ unless otherwise stated. In the current study we also consider fractional time intervals $[t_n, t_{n+1/2}]$ and $[t_{n+1/2}, t_{n+1}]$ with size $\Delta t/2$ to be used for the predictor and corrector stages, respectively. In what follows we describe the steps used in our meshless method for solving the convection–diffusion equation (1).

2.1. Radial basis functions

Let us assume a nodal distribution of M distinct points $\mathbf{x}_i$ is used as a collocation in the computational domain as shown in Fig. 1. In the present study, for each nodal point $\mathbf{x}_i$ we introduce mid collocation point denoted by $\mathbf{x}_{i+1/2}$. The starting point in the interpolation by local RBF is to interpolate the linear or nonlinear flux function $f(u_i,t)$ by the expansion

$$f(u_i,t) \simeq \sum_{j\in\mathcal{I}_{i,m}} \lambda_j(t)\varphi\Big(\big\|\mathbf{x}_i - \mathbf{x}_j\big\|\Big), \tag{4}$$

where $\mathcal{I}_{i,m}$ is a local set containing the index i and indices of the neighboring points to $\mathbf{x}_i$. In (4), λ_j's are the unknown coefficients to be calculated, $r_{ij} = \big\|\mathbf{x}_i - \mathbf{x}_j\big\|$ is the distance between the points $\mathbf{x}_i$ and $\mathbf{x}_j$, and $\varphi\left(\|\mathbf{x}_i - \mathbf{x}_j\|\right)$ is the radial basis function. Many radial basis functions exist in the literature and in the current study we consider the infinitely smooth multiquadrics radial basis function defined as

$$\varphi(r) = \sqrt{1+\epsilon^2 r^2}, \tag{5}$$

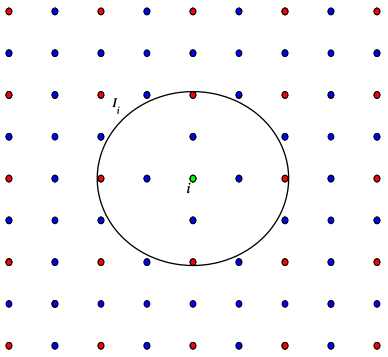

Fig. 1. Illustration of uniform collocation points covering the computational domain. Here, for a collocation point $\mathbf{x}_i$ the set I_i is shown and the blue points are used in the predictor stage whereas the corrector stage uses all the points in the set I_i. (For interpretation of the references to color in this figure legend, the reader is referred to the web version of this article.)

where $\epsilon \neq 0$ is the shape parameter controlling the fitting of a smooth surface to the data. Selection of optimal values for the shape parameter has been subject of several studies, see [15,6,11] among others. In the present work we used the following selection

$$\epsilon = 0.8\frac{\sqrt{n_s}}{d_m}, \tag{6}$$

with n_s is the cardinal number of the set $\mathcal{I}_{i,m}$ and d_m denotes the smallest nodal distance in $\mathcal{I}_{i,m}$. Note that other selections for the shape constant ϵ and other radial basis functions can easily be incorporated in our analysis without major conceptual modifications.

The selection of the set $\mathcal{I}_{i,m}$ may depend on the problem under study and for purpose of this study upwinding techniques are adopted for the selection of the set $\mathcal{I}_{i,m}$. Thus, for each collocation point $\mathbf{x}_i$ the associated set $\mathcal{I}_{i,m}$ contains the index i and indices of the m nearest neighboring points to $\mathbf{x}_i$. It is evident that for this selection the cardinal number of the set $\mathcal{I}_{i,m}$ is defined as $n_s = m+1$. Using this selection of the set $\mathcal{I}_{i,m}$ the expansion coefficients $\lambda_i(t)$ in (4) are obtained by solving the following linear system of $n_s \times n_s$ algebraic equations

$$\mathbf{B}^{[i]}\Lambda^{[i]} = \mathbf{f}(\mathbf{u})^{[i]}, \tag{7}$$

where $\mathbf{B}^{[i]}$ is an $n_s \times n_s$ matrix with entries $\varphi\left(\|x_i - x_j\|\right)$, $\Lambda^{[i]}$ and $\mathbf{f}(\mathbf{u})^{[i]}$ are n_s-valued vectors with entries λ_i and $f(u_i)$, respectively. For the choice of radial basis function φ in (5), the interpolation matrix $\mathbf{B}^{[i]}$ in (7) is guaranteed to be nonsingular for any set of distinct points and the invertibility is therefore guaranteed, see for example [19,21].

Because of the linearity of the linear combination (4), time and space derivatives of the interpolant (4) may be calculated in a straightforward manner. For instance, the temporal and first-order spatial derivatives at the points $\mathbf{x}_i$ can be calculated as

$$\frac{\partial f(u)}{\partial t} = \sum_{j\in\mathcal{I}_{i,m}} \frac{\partial \lambda_j}{\partial t}\varphi\Big(\big\|\mathbf{x}_i - \mathbf{x}_j\big\|\Big), \qquad \frac{\partial f(u)}{\partial x} = \sum_{j\in\mathcal{I}_{i,m}} \lambda_j(t)\frac{\partial \varphi}{\partial x}\Big(\big\|\mathbf{x}_i - \mathbf{x}_j\big\|\Big),$$
$$\frac{\partial f(u)}{\partial y} = \sum_{j\in\mathcal{I}_{i,m}} \lambda_j(t)\frac{\partial \varphi}{\partial y}\Big(\big\|\mathbf{x}_i - \mathbf{x}_j\big\|\Big).$$

Similarly to (7), the partial derivatives can also be written in a compact matrix form as

$$\frac{\partial \mathbf{f}(\mathbf{u})^{[i]}}{\partial t} = \mathbf{B}^{[i]}\frac{\partial \Lambda^{[i]}}{\partial t}, \qquad \frac{\partial \mathbf{f}(\mathbf{u})^{[i]}}{\partial x} = \mathbf{H}_x^{[i]}\Lambda^{[i]}, \qquad \frac{\partial \mathbf{f}(\mathbf{u})^{[i]}}{\partial y} = \mathbf{H}_y^{[i]}\Lambda^{[i]},$$

where $\mathbf{H}_x^{[i]}$ and $\mathbf{H}_y^{[i]}$ are n_s-valued row matrices with entries $\frac{\partial\varphi}{\partial x}\left(\|\mathbf{x}_i - \mathbf{x}_j\|\right)$ and $\frac{\partial\varphi}{\partial y}\left(\|\mathbf{x}_i - \mathbf{x}_j\|\right)$, respectively. Using Eq. (7), the spatial derivatives can also be reformulated as

$$\frac{\partial \mathbf{f}(\mathbf{u})^{[i]}}{\partial x} = \mathbf{H}_x^{[i]}\left(\mathbf{B}^{[i]}\right)^{-1}\mathbf{f}(\mathbf{u})^{[i]}, \qquad \frac{\partial \mathbf{f}(\mathbf{u})^{[i]}}{\partial y} = \mathbf{H}_y^{[i]}\left(\mathbf{B}^{[i]}\right)^{-1}\mathbf{f}(\mathbf{u})^{[i]}.$$

Note that for time-dependent convection–diffusion problems of type (1), the spatial derivatives need to be evaluated several times during the time integration procedure. Therefore, for efficiency reason, global spatial derivative matrices $\mathbf{D}_x$ and $\mathbf{D}_y$ are formed once and the derivatives can be evaluated by a single matrix by vector multiplication as

$$\frac{\partial \mathbf{f}(\mathbf{u})}{\partial x} = \mathbf{D}_x \mathbf{f}(\mathbf{u}), \qquad \frac{\partial \mathbf{f}(\mathbf{u})}{\partial y} = \mathbf{D}_y \mathbf{f}(\mathbf{u}). \tag{8}$$

Here, the derivative matrix $\mathbf{D}_x$ is an $M \times M$ matrix the entries of which are $n_s \times n_s$ sub-matrices $\mathbf{d}_{ij}$ defined as

$$\mathbf{d}_{ij} = \begin{cases} \mathbf{H}_x^{[i]} \left(\mathbf{B}^{[i]}\right)^{-1}, & \text{if } j \in \mathcal{I}_{i,m}, \\ \mathbf{0}, & \text{if } j \notin \mathcal{I}_{i,m}, \end{cases}$$

with $i = 1, \ldots, M$. The derivative matrix $\mathbf{D}_y$ can be formulated in a similar manner as for the matrix $\mathbf{D}_x$. The second-order spatial derivatives can be approximated using the same procedure and we denote by $\mathbf{D}_{xx}$ and $\mathbf{D}_{yy}$ the derivative matrices associated with $\frac{\partial^2}{\partial x^2}$ and $\frac{\partial^2}{\partial y^2}$, respectively.

It should be stressed that a direct application of the RBF method for solving convection-dominated flow problems results in oscillatory and unstable solutions independently of the number of collocation points and the CFL condition used in the simulations. In the current work, to stabilize the RBF solution for the convection–diffusion problem (1) we consider a predictor–corrector approach. In the predictor stage, predicted values of the solution are computed on the blue midpoint nodes at time $t_n + \alpha \Delta t$. To do this, we solve at these midpoint nodes a transport equation using the modified method of characteristics (MMC) applied at the convection part in (2). We find the backward characteristic foot X_0 corresponding to a given blue node. Since the solution is constant on a characteristic, the solution in a midpoint blue node at time $t_n + \alpha \Delta t$ is equal to the solution at time t_n in the point X_0. This one is evaluated by a RBF interpolation process. At the corrector stage, the solution in the reference node must be calculated for the stage $n + 1$. Therefore, the numerical fluxes are approximated on the reference node using the interpolated solutions at the characteristics feet using the midpoints stencil $I_{i+1/2,m}$. Then, the solution at the reference node can be calculated using the first order Euler scheme and adding the diffusion part of Eq. (1).

2.2. The predictor stage

Following for example [22,9], the characteristic curves of Eq. (2) are the solution of initial value problem for ordinary differential equations

$$\begin{aligned} \frac{d\mathbf{X}_{i+1/2}(\tau)}{d\tau} &= \mathbf{v}\big(\tau, \mathbf{X}_{i+1/2}(\tau)\big), \quad \tau \in [t_n, t_{n+1}], \\ \mathbf{X}_{i+1/2}(t_{n+1}) &= \mathbf{x}_{i+1/2}. \end{aligned} \tag{9}$$

Note that $\mathbf{X}_{i+1/2}(\tau; t_{n+1}, \mathbf{x}_{i+1/2}) = \big(X_{i+1/2}(\tau; t_{n+1}, \mathbf{x}_{i+1/2}), Y_{i+1/2}(\tau; t_{n+1}, \mathbf{x}_{i+1/2})\big)^T$, is the departure point at time τ of a particle that will arrive at $\mathbf{x}_i$ at time t_{n+1}. The MMC does not follow the flow particles forward in time, as the Lagrangian schemes do, instead it traces backwards the position at time t_n of particles that will reach the points of a fixed collocation point at time t_{n+1}. By so doing, the MMC avoids the solution distortion difficulties that the conventional Lagrangian schemes have. The solutions of (9) can be expressed as

$$\begin{aligned} X_{i+1/2}(t_n) &= x_{i+1/2} - \int_{t_n}^{t_{n+1/2}} \mathbf{v}_{i+1/2}\Big(\tau, X_{i+1/2}(\tau)\Big)\, d\tau, \\ &\coloneqq x_{i+1/2} - \delta_{i+1/2}. \end{aligned} \tag{10}$$

It is worth remarking that the departure points in (10) are calculated in the interval $[t_n, t_{n+1/2}]$ instead of $[t_n, t_{n+1}]$. This is motivated by the idea of reconstructing a predictor–corrector scheme where the predictor stage is computed at the fractional time $t_{n+1/2}$ completed by a corrector stage computed at the end time t_{n+1}. This fractional time stepping is also supported by the analysis reported in [4].

To compute the displacement $\delta_{j,i+1/2}$ in (10) we consider the following iterations

$$\begin{aligned}\delta_{i+1/2}^{(0)} &= \frac{\Delta t}{4}\mathbf{v}_{i+1/2}\left(t_n, x_{i+1/2}\right),\\ \delta_{i+1/2}^{(k)} &= \frac{\Delta t}{4}\mathbf{v}_{i+1/2}\left(t_n, x_{i+1/2}-\delta_{i+1/2}^{(k-1)}\right), \quad k=1,2,\ldots.\end{aligned} \tag{11}$$

Once the characteristic curves $X_{i+1/2}(t_n)$ are known, a solution at the collocation point $x_{i+1/2}$ is reconstructed as

$$\begin{aligned}\mathbf{u}_{i+1/2}^n &= \mathbf{u}\left(t_{n+1/2}, x_{i+1/2}\right),\\ &= \mathbf{u}\left(t_n, X_{i+1/2}(t_n)\right),\\ &:= \widetilde{\mathbf{u}}_{i+1/2}^n,\end{aligned} \tag{12}$$

where $\widetilde{\mathbf{u}}_{i+1/2}^n$ is the solution at the characteristic foot $X_{i+1/2}(t_n)$ computed by interpolation from the collocation points in the set $\widehat{I}_{i,m}$ where the departure point resides *i.e.*

$$\widetilde{\mathbf{u}}_{i+1/2}^n = \widehat{\mathbf{R}}^{[i+1/2]}\mathbf{u}^n, \tag{13}$$

where $\widehat{\mathbf{R}}^{[i+1/2]}$ is ith row of the RBF interpolation matrix which is formulated as follows.

To interpolate solution at the characteristics foot $X_{i+1/2}(t_n)$ using RBF method, one assumes that

$$\widetilde{\mathbf{u}}_{i+1/2}^n = \sum_{j\in I_{i,m}} \lambda_j(t)\varphi(\|X_{i+1/2}-x_j\|,\varepsilon),$$

where $I_{i,m}$ contains the collocation points surrounding $X_{i+1/2}$. The expansion coefficients λ_j's are determined by imposing the interpolation condition at all the points x_j contained in the local support $I_{i,m}$ as

$$\widetilde{\mathbf{u}}_j^n = \sum_{k\in\mathcal{I}_{i,m}} \lambda_j(t)\varphi(\|x_j-x_k\|,\varepsilon) = u(x_j).$$

This results to a linear system to be solved for λ_j's as in Eq. (7). Local expansion coefficients are determined by matrix inversion and the interpolant of the solution is expressed as

$$\widetilde{\mathbf{u}}_{i+1/2}^n = \mathbf{h}^{[i+1/2]}\mathbf{\Lambda}^{[i]} = h^{[i+1/2]}\left(\mathbf{B}^{[i]}\right)^{-1}\mathbf{u}^{[i]}, \tag{14}$$

where $\mathbf{B}^{[i]}$ is the same $m\times m$ local distance matrix defined in (7) and $h^{[i+1/2]}$ is a m-valued line-vector defined by

$$\mathbf{h}_j^{[i+1/2]} = \varphi(\|X_{i+1/2}-x_j\|,\varepsilon).$$

The ith row of the global RBF interpolation matrix, $\widehat{\mathbf{R}}$ is formulated as follows:

$$\widehat{\mathbf{R}}_j^{[i+1/2]} = \begin{cases}\mathbf{h}^{[i+1/2]}\left(\mathbf{B}^{[i]}\right)_j^{-1}, & \text{if } j\in\mathcal{I}_{i,m},\\ \mathbf{0}, & \text{if } j\notin\mathcal{I}_{i,m}.\end{cases}$$

2.3. The corrector stage

Applied to the diffusion part in (1), the meshless RBF method approximates the solution u_i at each collocation point $\mathbf{x}_i$, $i=1,2,\ldots,M$ as

$$u_i(t) := u(t,\mathbf{x}_i) = \sum_{j\in\mathcal{I}_{i,m}} \lambda_j(t)\varphi\Big(\big\|\mathbf{x}_i-\mathbf{x}_j\big\|\Big). \tag{15}$$

Inserting the above expansion in (1) and using the spatial derivative matrices, the formulation of the system (1) can be obtained as

$$\mathbf{u}_i^{n+1} = \widetilde{\mathbf{u}}_{i+1/2}^n - \Delta t\mathbf{v}_{i+1/2}^n\cdot\left(\nabla^{[i+1/2]}\widetilde{\mathbf{u}}^n\right) + \Delta t\nu\left(\mathbf{D}_{xx}^{[i]}\mathbf{u}^n + \mathbf{D}_{yy}^{[i]}\mathbf{u}^n\right), \tag{16}$$

where $\nabla^{[i+1/2]}$ is composed by the ith rows of the gradient RBF matrices $\mathbf{D}_x$ and $\mathbf{D}_y$ in (8) associated with the mid collocation points $x_{i+1/2}$, $\mathbf{D}_{xx}^{[i]}$ and $\mathbf{D}_{yy}^{[i]}$ are the ith rows of the RBF matrices $\mathbf{D}_{xx}$ and $\mathbf{D}_{yy}$ associated with the collocation points x_i. In (16), the solutions $\mathbf{u}$ and $\widetilde{\mathbf{u}}$ are vectors with entries u_i and $\widetilde{u}_i$, respectively. Note that the time discretization (16) is only first-order accurate. However, other high-order time stepping schemes can be applied without major conceptual modifications.

In summary, the implementation of our RBF algorithm to solve the convection–diffusion equation (1) is carried out in the following steps:

1. *Compute the departure points* $X_{i+1/2}(t_n)$ *associated with the material derivative* (3) *using the iterative procedure* (10)–(11).
2. *Compute the approximations* $\widetilde{u}_{i+1/2}^n = u\left(t_n, X_{i+1/2}(t_n)\right)$ *employing the interpolation procedure* (13).
3. *Update the solutions* u_i^{n+1} *using* (16).

Note that, since the radial basis functions are time-independent, the system matrix of the linear system resulting from the proposed RBF method is also time-independent. A major advantage is then the ability to retain the system matrix assembled at the first time step to be reused at later time steps without alteration. This is achieved by factorizing the system matrix using an $\mathsf{LDL}^\top$ decomposition where L is a lower and D is a diagonal matrix. This factorization is only done at the first time step while resolving the system is reduced to forward-, diagonal- and backward-substitutions at any time step after updating the right-hand side of the system. This can significantly increase the efficiency when a large number of time steps is needed, compared to updating the matrix and fully solving the system if a time-dependent radial basis functions are to be used. It should also be stressed that to solve the linear systems resulted from the RBF method we used the Singular Value Decomposition (SVD) algorithm [14]. The performance of the SVD solver for solving highly ill-conditioned systems as those obtained in the current study is commonly well-established.

3. Numerical results

We present numerical results for a linear passive advection–diffusion of a Gaussian pulse problem and for a nonlinear viscous Burgers. For these test examples the analytical solution is known, so that we can evaluate the error function $\mathbf{e} = \mathbf{e}(t_n)$ at time t_n as

$$e_i^n = u_i^n - u(t_n, \mathbf{x}_i), \tag{17}$$

where $u(t_n, \mathbf{x}_i)$ and u_i^n are the exact and numerical solutions, respectively, at collocation point $\mathbf{x}_i$ and time t_n. The following discrete error-norms are defined

$$\|\mathbf{e}\|_{L^1} = \sum_i |e_i|, \qquad \|\mathbf{e}\|_{L^2} = \left(\sum_i |e_i|^2\right)^{\frac{1}{2}}.$$

Furthermore, we define the CFL number associated to (1) as follows

$$\mathrm{CFL} = \max\left(|v_1|, |v_2|\right) \frac{\Delta t}{d_{\min}}, \tag{18}$$

where $d_{\min}$ denotes the smallest nodal distance in all collocation points. In all our simulations, the CFL number is fixed to 0.85 and the time step Δt is adjusted according to (18).

3.1. Gaussian pulse problem

This example solves the advection–diffusion problem of rotating a Gaussian pulse extensively used in the literature to test the accuracy of transport methods such us the semi-Lagrangian (SLAG) method, see for example [22,29,10]. The equations are of the form (1) with $\mathbf{v} = (-4y, 4x)^T$. Initial and boundary conditions are taken from the analytical solution

$$u(t, x, y) = \frac{\sigma^2}{\sigma^2 + 4\nu t} \exp\left(-\frac{(\bar{x} - x_0)^2 + (\bar{y} - y_0)^2}{\sigma^2 + 4\nu t}\right),$$

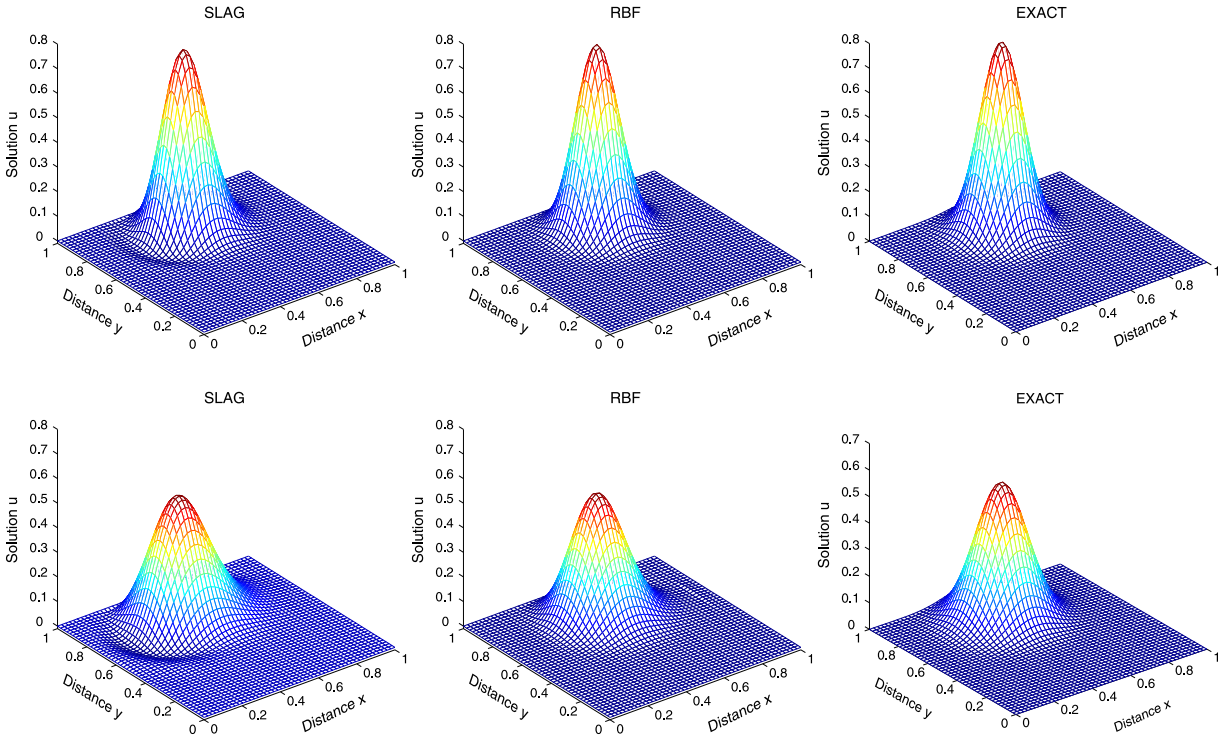

Fig. 2. Results for the Gaussian pulse problem after 1 revolution (first row) and 3 revolution (second row) using 50×50 collocation points.

where $\bar{x} = x\cos(4t) + y\sin(4t)$, $\bar{y} = -x\sin(4t) + y\cos(4t)$, $x_0 = 0.5$, $y_0 = 0.75$ and $\sigma^2 = 0.002$. The computational domain is $[0, 1] \times [0, 1]$ and the time period required for one complete rotation is $\frac{\pi}{2}$. In all our simulations for this test example, a set of 50×50 collocation points is used and the diffusion coefficient is set to $\nu = 10^{-3}$. The purpose of this advection–diffusion problem is to compare the numerical results obtained using our RBF method to those computed using the mesh-based SLAG method.

In Fig. 2 we display the numerical results computed using the RBF scheme after 1 revolution and 3 revolutions. In Fig. 3 we present the associated 10 equi-distributed contour lines of these solutions. For comparison reasons, we have also included in these figures the computational resulted obtained using the conventional SLAG scheme and the analytical solutions using a mesh of 50×50 gridpoints. The one-dimensional plots in Fig. 4 correspond to a cross-section at the horizontal line with $y = 0.75$ of the results obtained after 1 revolution and 3 revolutions. A visual comparison of the results in these figures shows severe numerical dissipation, overshoot, deformation and phase errors in the numerical solutions obtained using the SLAG method. For instance, SLAG results after 3 revolutions exhibit nonphysical oscillations and substantially greater distortion, specially at the feet of the Gaussian pulse where the gradient is relatively sharp. From the same figures we observe an absence of these oscillations in the numerical results obtained using the RBF method. It is evident that, after one revolution, both methods give roughly similar results with some small differences on the maximum value of the numerical solutions. However, by increasing the number of revolutions to 3, the RBF results are more accurate than those of the conventional SLAG method. It is clear that the RBF scheme performs best for this test example. It should be pointed out that rotating the Gaussian pulse for more than 3 revolutions results in nonphysical solutions for the SLAG method whereas the RBF scheme still produces satisfactory results.

To present a quantitative comparison of the results computed by the RBF and SLAG methods we summarize in Table 1 the L^1 and L^2 errors, the minimum (min) and maximum (max) values of the computed solutions. We present numerical results after 1 and 3 revolutions using three numbers of points in the mesh for SLAG method and in the collocation sets for RBF method. In terms of the L^1 and L^2 errors the RBF results are more accurate than the results obtained using the conventional SLAG method for considered collocations sets. From the values of max and min in Table 1 we observe high and negative values for the conventional SLAG results that are avoided in the RBF results.

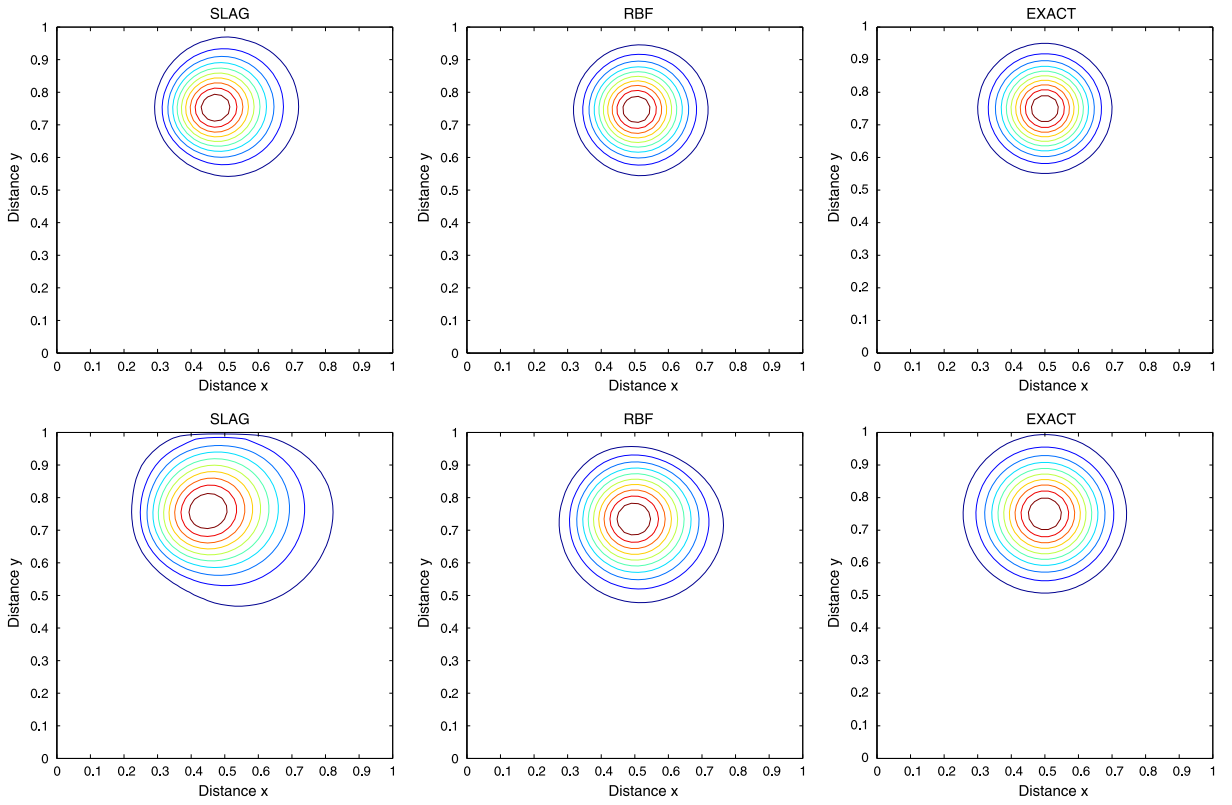

Fig. 3. Results for the Gaussian pulse problem after 1 revolution (first row) and 3 revolution (second row) using 50×50 collocation points.

Table 1
Results for the Gaussian pulse problem after 1 and 3 revolutions. Note that the analytical maximum after 1 revolution is 0.75 and after 3 revolutions is 0.5.

Method	Points	min	max	L^1-error	L^2-error
		After 1 revolution			
RBF	50×50	-0.00004835	0.743688	0.00077532	0.00046215
	100×100	-0.00002492	0.750814	0.00034651	0.00024431
	200×200	-0.00000295	0.747554	0.00016793	0.00013205
SLAG	50×50	-0.01231785	0.735426	0.00713903	0.00668748
	100×100	-0.00027517	0.758223	0.00278025	0.00241946
	200×200	-0.00006934	0.760817	0.00287571	0.00200973
		After 3 revolutions			
RBF	50×50	-0.00014402	0.496551	0.00097533	0.00086411
	100×100	-0.00005921	0.500914	0.00044708	0.00031209
	200×200	-0.00000576	0.496684	0.00020654	0.00014327
SLAG	50×50	-0.02678958	0.491842	0.01476431	0.01145755
	100×100	-0.00083346	0.521730	0.00602190	0.00518927
	200×200	-0.00022091	0.524413	0.00537023	0.00478164

3.2. Burgers flow problem

In this example we consider the following Burgers equation which evolves to a highly convective steady state

$$\frac{\partial u}{\partial t} + \lambda y \left(u - \frac{1}{2}\right) \frac{\partial u}{\partial x} + \lambda x \left(u - \frac{1}{2}\right) \frac{\partial u}{\partial y} - \Delta u = 0,$$

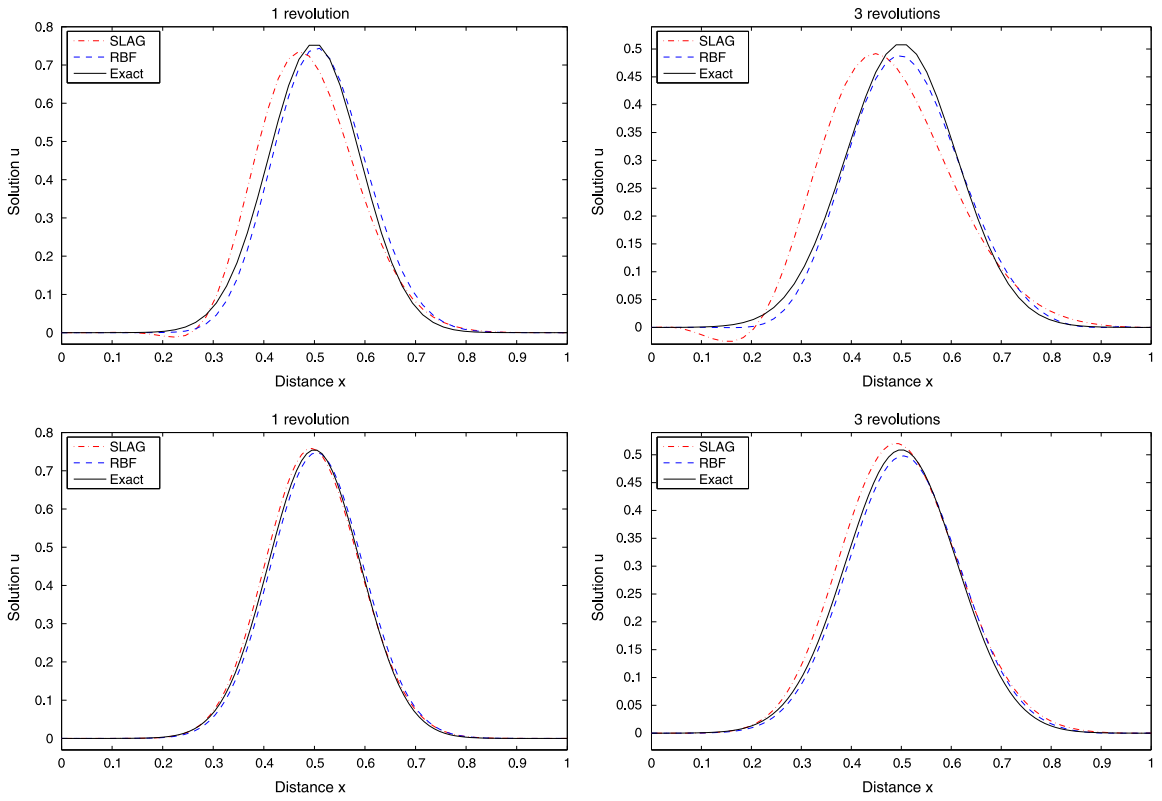

Fig. 4. Cross-sections at $y = 0.75$ of the results for the Gaussian pulse problem after 1 revolution (left) and 3 revolutions (right) using 50×50 collocation points (first row) and 100×100 collocation points (second row).

where λ is a constant controlling the magnitude of the nonlinear convective terms [18]. The boundary conditions are Dirichlet given by the exact steady state solution

$$u(x, y) = \frac{1}{2}\left(1 - \tanh\left(\frac{\lambda x y}{2}\right)\right).$$

We first solve this problem in the squared domain $\Omega = [-5, 5] \times [-5, 5]$. To define initial conditions for this problem we first divide the domain into four equally sub-squares as: $\Omega_1 = [-5, 0] \times [-5, 0]$, $\Omega_2 = [-5, 0] \times [0, 5]$, $\Omega_3 = [0, 5] \times [-5, 0]$ and $\Omega_4 = [0, 5] \times [0, 5]$. Then, the solution is alternated between these sub-squares as follows:

$$u(0, x, y) = \begin{cases} 0, & \text{if } (x, y) \in \Omega_1 \cup \Omega_4, \\ 1, & \text{if } (x, y) \in \Omega_2 \cup \Omega_3, \\ \frac{1}{2}, & \text{if } x = 0 \text{ or } y = 0. \end{cases} \tag{19}$$

We used our RBF method to compute the steady-state solutions for three different values of λ namely, $\lambda = 1$, $\lambda = 5$ and $\lambda = 10$. This test example has been solved in [18] using the conventional finite element SLAG method and therefore, these results are compared to those obtained using our RBF method.

Fig. 5 illustrates the obtained steady-state solutions obtained using the RBF and SLAG methods along with the analytical steady-state solutions using a mesh of 50×50 gridpoints. The collocation points for the RBF method are uniformly distributed in the computational domain. In Fig. 6 we plot 10 equi-distributed contours of the corresponding results. It is clear that, by increasing the values of λ the convective terms become larger and steep boundary layers are formed near the vicinity of center lines in the computational domain. For low values of λ, the boundary layers are wide and diffuse in the flow domain. As λ increases, the boundary layers concentrate and move towards the domain center. It is apparent that the solution structures are in good agreement with the previous work in [18]. These plots give a clear view of the overall flow pattern and the effect of the convection control parameter λ on the structure of steady

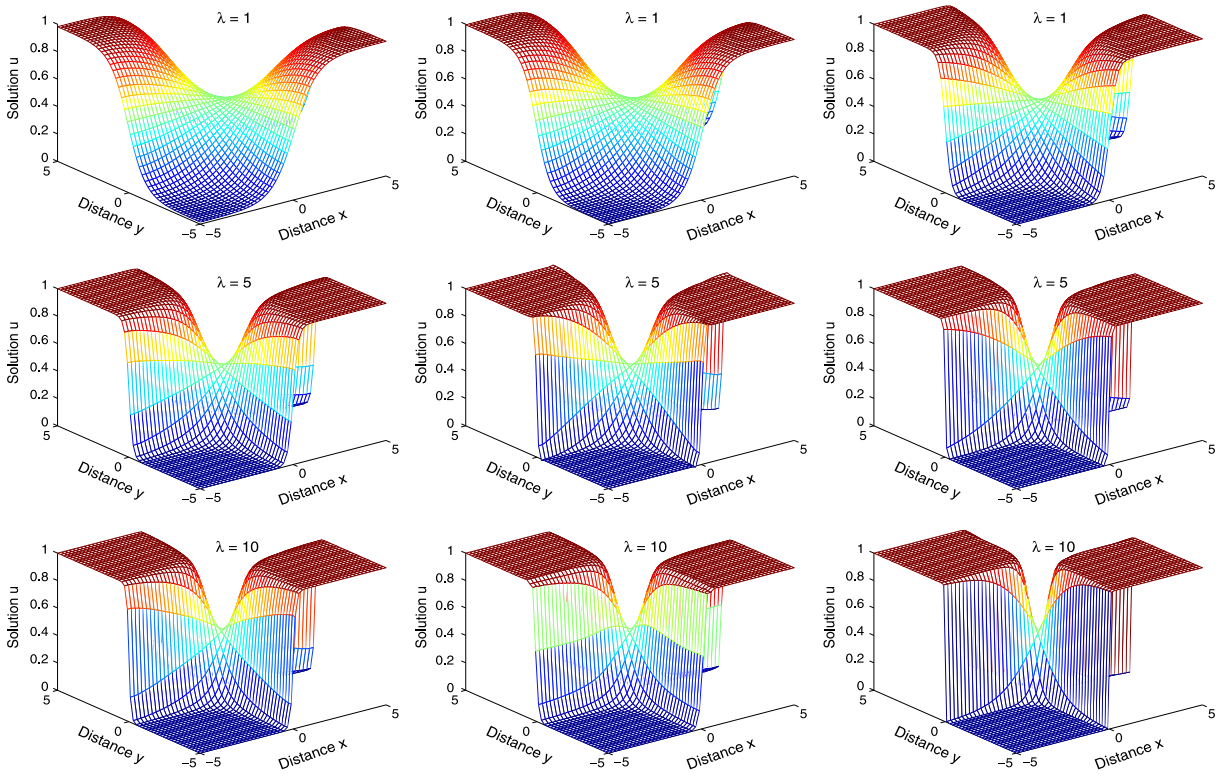

Fig. 5. Results for the Burgers flow problem at different values of λ using the SLAG method (first column), RBF method (second column) and exact solution (third column) on a collocation set of 50 × 50 points.

boundary layers in the cavity. It is worth remarking that the thinning of the boundary layers with increasing λ is evident from these plots, although the rate of this thinning is slower for the SLAG method than for the RBF method. These features clearly demonstrate the high accuracy achieved by the proposed RBF method for solving viscous Burgers problems at steady-state regimes. In addition, compared to the results published for example in [18], it can be seen that our RBF method resolves accurately the solution features and the boundary layers seem to be localized in the correct place in the flow domain.

To further visualizing the comparisons, we display in Fig. 7 cross-sections at the main diagonal using two collocation sets with 50 × 50 and 200 × 200 points. For consistency, same numbers of gridpoints are used in meshes for the SLAG method. For $\lambda = 10$, it is clear that the SLAG and RBF methods produce practically identical results on the mesh of 200×200 nodes. This can be attributed to the small physical diffusion presented in the problem. However, decreasing the value of λ to 5 or 1 the results computed by RBF method are more accurate than those computed by the SLAG method. Apparently, by using the RBF method, high resolution is achieved in those regions where the flow gradients are steep such as the moving fronts. Comparing the results obtained using the considered methods, it is clear that the SLAG method produces diffusive solutions resulting in smearing the shocks. On the other hand, this numerical diffusion has remarkably been reduced in the results computed using the RBF method. Needless to say that for convection-dominated situation, the RBF method does not diffuse the fronts or gives spurious oscillations near the steep gradients. Our RBF method accurately approximates the numerical solution to this steady-state flow problem. The results shown here compare favorably with those published in the literature for the viscous Burgers problems, see for instance [18].

Next we solve the above Burgers flow problem in a circular domain centered in (0, 0) and with radius 5. The initial conditions are the same as before and given by (19). We also consider the same values for the convection coefficient $\lambda = 1$ and $\lambda = 5$ as in the previous test example. It should be stressed that, since the RBF method is a collocation method, the distribution of collocation points in the computational domain would influence the accuracy of its results.

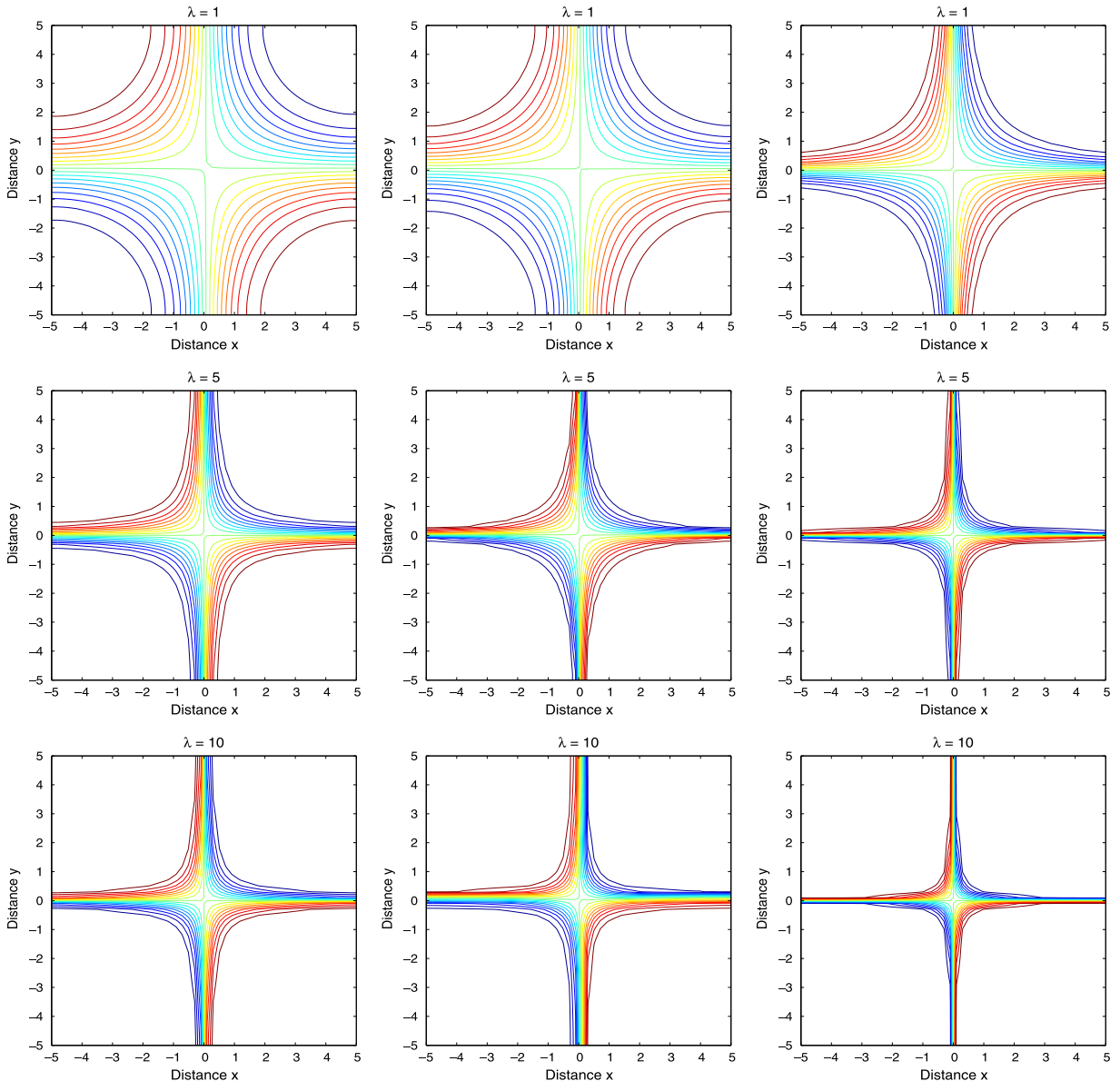

Fig. 6. Results for the Burgers flow problem using different values of λ using the SLAG method (first column), RBF method (second column) and exact solution (third column) on a mesh of 50 × 50 collocation points.

To illustrate this effect for this test example, we consider two collocation sets of points namely Uniform distribution and Halton distribution as depicted in Fig. 8. The total number of points for each collocation set is 1663 for both the Uniform distribution and Halton distribution. It is clear that the total numbers of collocation points are the same for both sets but their distributions are completely different.

In Fig. 9 we illustrate the obtained results at steady-state regime using the considered collocation sets. It can be clearly seen that the complicated solution structures are being captured by the RBF method. However, the results obtained using the Uniform distribution exhibits better resolution compared to those obtained using the Halton distribution. It should be pointed out that for small values of the convection coefficient λ the RBF method exhibits similar results for both distributions. However, for large values of λ the accuracy of RBF method using the Halton distribution is deteriorated. The results shown here compare favorably with those obtained for the same flow problem on a squared domain. For a better insight we present in Fig. 10 cross-sections of the results along the diagonal line

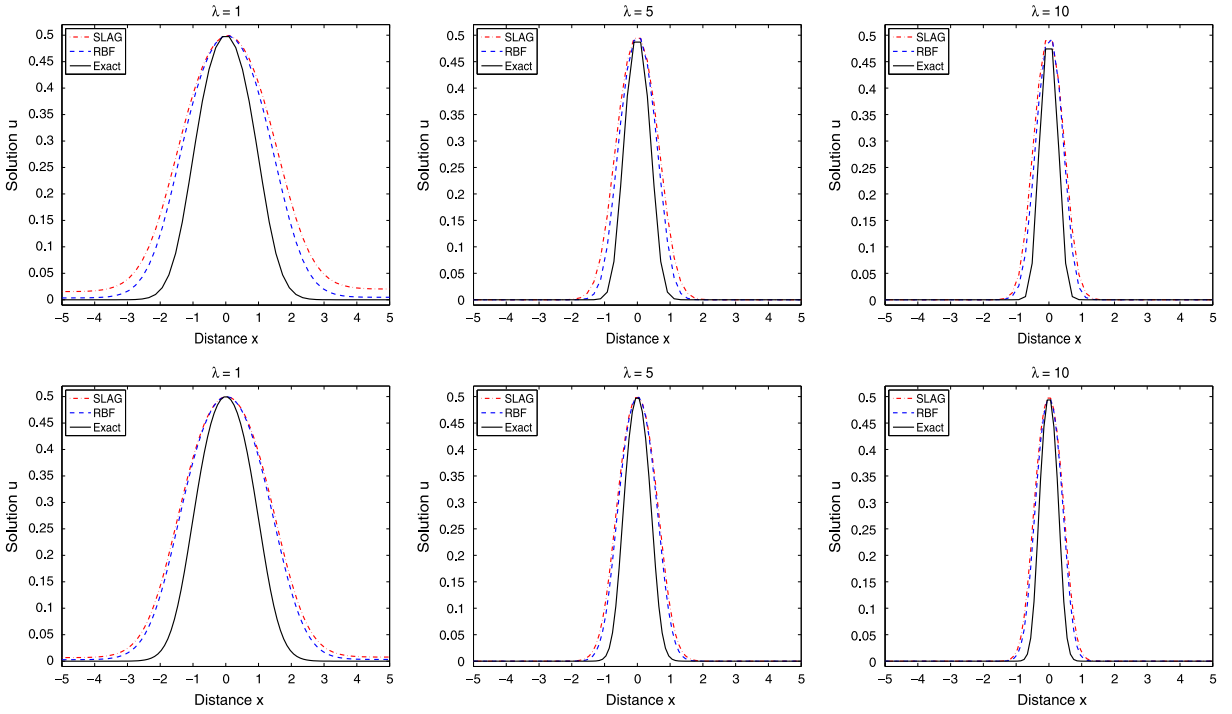

Fig. 7. Cross sections at $y = x$ of the results for the Burgers flow problem using 50×50 collocation points (first row) and 200×200 collocation points (second row).

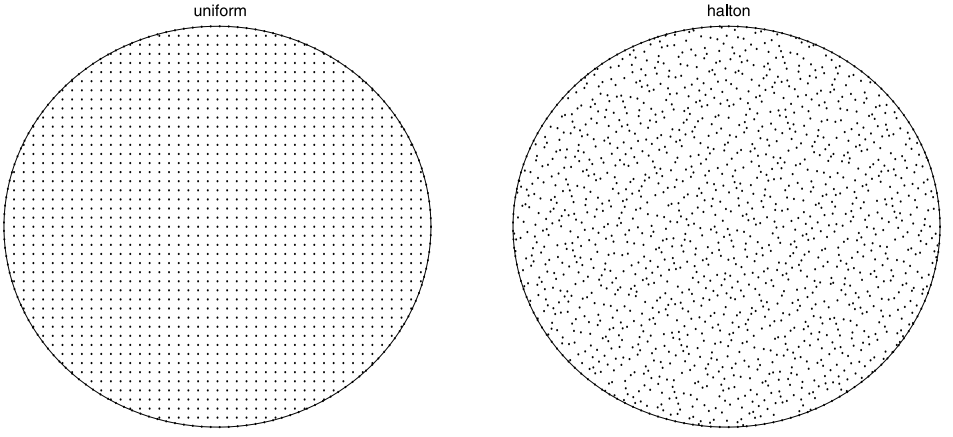

Fig. 8. Sets of collocation points used for the Burgers flow problem in a circular domain.

shown in Fig. 9. It is clear that, for $\lambda = 5$, the computed results on Halton distribution are more diffusive than those computed using the Uniform distribution. Compared to the numerical results obtained using $\lambda = 1$, the RBF method shows no sensibility to the qualitative distribution of the collocation points in the computational domain. Overall, the proposed RBF method demonstrates its ability to capture the correct dynamics for this test example. No extensive numerical dissipation has been detected in the results obtained using the RBF method. Furthermore, the obtained results for the considered flow problem demonstrate the ability of the presented RBF method to capture the small solution features within the computational domain without generating nonphysical oscillations.

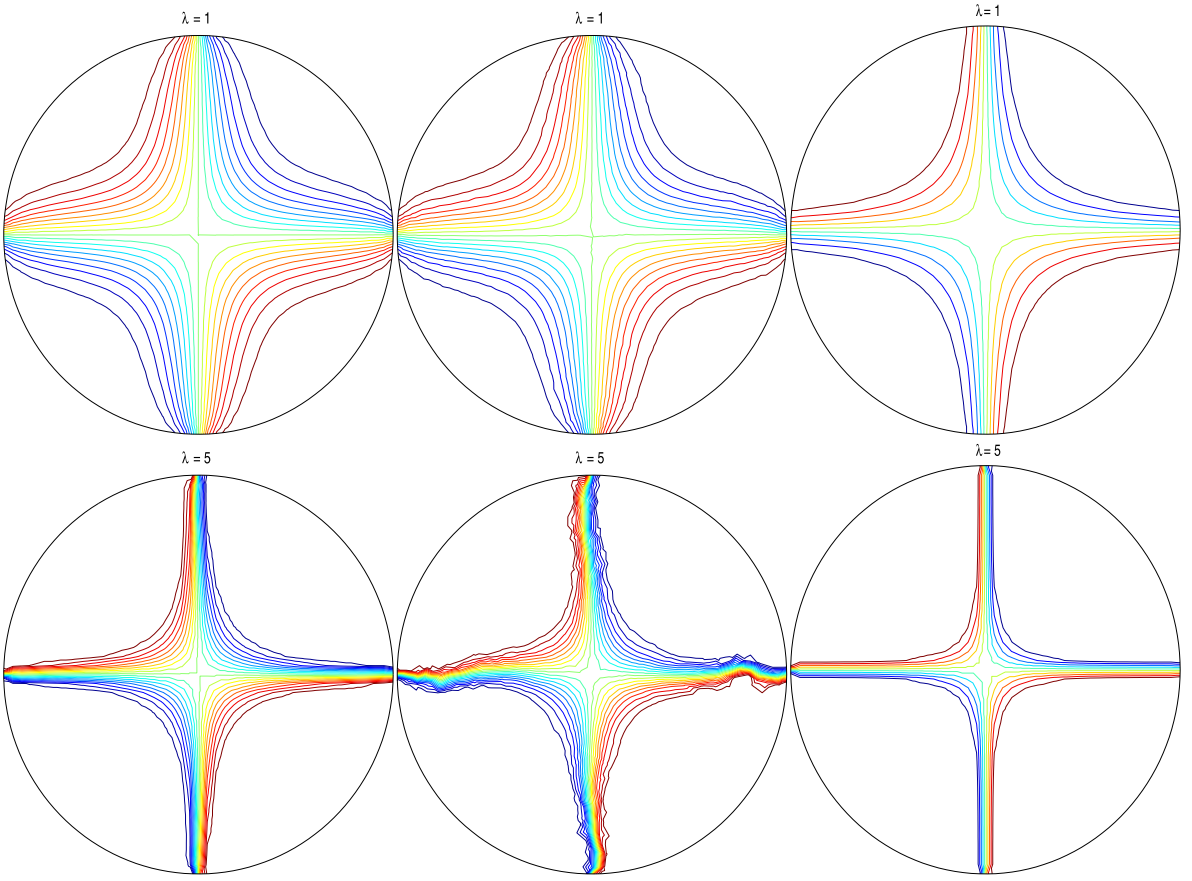

Fig. 9. Results for the Burgers flow problem in a circular domain using different values of λ using the uniform (first column), Halton (second column) and exact solution (third column).

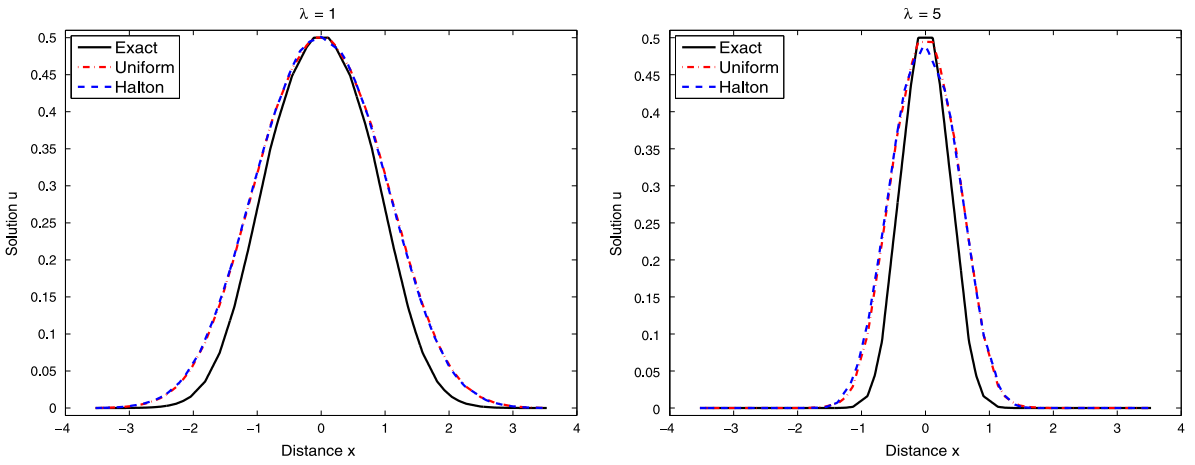

Fig. 10. Cross sections at $y = x$ of the results for the Burgers flow problem in a circular domain using $\lambda = 1$ (left) and $\lambda = 5$ (right).

3.3. Incompressible Navier–Stokes problem

In what follows we test the ability of the new RBF to solve incompressible Navier–Stokes equations. These nonlinear problems are not easy to solve since the velocity field depends on the solution itself rather than the time and

Table 2
Values of stream function and vorticity at the center of the primary vortex for the lid-driven cavity flow.

Re	Ghia et al. [12]			RBF method		
	ψ	ω	Location (x, y)	ψ	ω	Location (x, y)
100	−0.103	3.166	(0.6172,0.7344)	−0.100	3.173	(0.6179,0.7353)
1 000	−0.117	2.049	(0.5313,0.5625)	−0.113	2.101	(0.5322,0.5619)
10 000	−0.119	1.880	(0.5117,0.5333)	−0.115	1.892	(0.5109,0.5326)

space variables. Let us consider the incompressible Navier–Stokes equations

$$\begin{aligned} \frac{\partial \mathbf{u}}{\partial t} + \mathbf{u} \cdot \nabla \mathbf{u} + \nabla p - \nu \Delta \mathbf{u} &= 0, \\ \nabla \cdot \mathbf{u} &= 0, \end{aligned} \tag{20}$$

where $\mathbf{u} = (u, v)^T$ is velocity field and p denotes the pressure. An alternative convection–diffusion formulation in terms of vorticity and stream function can be constructed as

$$\frac{\partial \omega}{\partial t} + u \frac{\partial \omega}{\partial x} + v \frac{\partial \omega}{\partial y} - \nu \Delta \omega = 0, \tag{21}$$

where the vorticity, ω, and stream function, ψ, are given by

$$\omega = \frac{\partial v}{\partial x} - \frac{\partial u}{\partial y}, \qquad u = \frac{\partial \psi}{\partial y}, \quad \text{and} \quad v = -\frac{\partial \psi}{\partial x}, \tag{22}$$

together with the following Poisson problem

$$\Delta \psi = -\omega. \tag{23}$$

Hence, the new RBF is applied to the convection–diffusion equation (21). We consider the standard problem of driven cavity flow intensively studied in [12]. The flow domain is $[0, 1] \times [0, 1]$ and the upper boundary moves with the velocity $u = 1$. Then the Reynolds number is defined as $Re = \frac{1}{\nu}$. We impose the no-slip boundary condition. We use a uniform collocation points with spacing $d_{\min} = \frac{1}{128}$ and we compute the steady state solution for $Re = 100$, $Re = 1000$ and $Re = 10\,000$. The obtained results for stream function and velocity field are shown in Fig. 11. Compared to the results published in [12], it can be seen that our new RBF resolves accurately the flow structures and the vortices seem to be localized in the correct place in the flow domain. The plots of streamline and velocity fields give a clear view of the overall flow pattern and the effect of the Reynolds number on the structure of the steady recirculating eddies in the cavity. In addition to the primary, center vortex, a pair of counterrotating eddies of a much smaller strength develop in the lower corners of the cavity. At $Re = 10\,000$, a third secondary vortex is seen in the upper left corner and a tertiary vortex in the lower right corner appears. It is apparent that the flow structure is in good agreement with the previous work [12].

For a low Re, the center of the primary vortex is located at the mid width and at about one-third of the cavity depth from the top. As the Re increases, the primary vortex center moves the right and becomes increasingly circular. Finally, with increasing Re this center moves down towards the geometric center of the cavity and becomes fixed in its location for $Re = 10\,000$. Values of stream function and vorticity at the center of primary vortices for different Reynolds numbers are compared in Table 2 with numerical results by Ghia et al. [12]. Good agreement is obtained.

4. Conclusions

A new stabilized meshless method has been proposed for the numerical solution of convection-dominated flow problems. This class of problems includes viscous Burgers equations and incompressible Navier–Stokes equations at high Reynolds numbers. The numerical method consists of a predictor and corrector stage using radial basis functions in both stages. To deal with the convection part in the governing equations the modified method of characteristics is also used in the predictor stage to stabilize conventional radial basis functions. Compared to the standard mesh-based methods applied to the same problem, our meshless method offers numerical techniques which are on one hand mesh

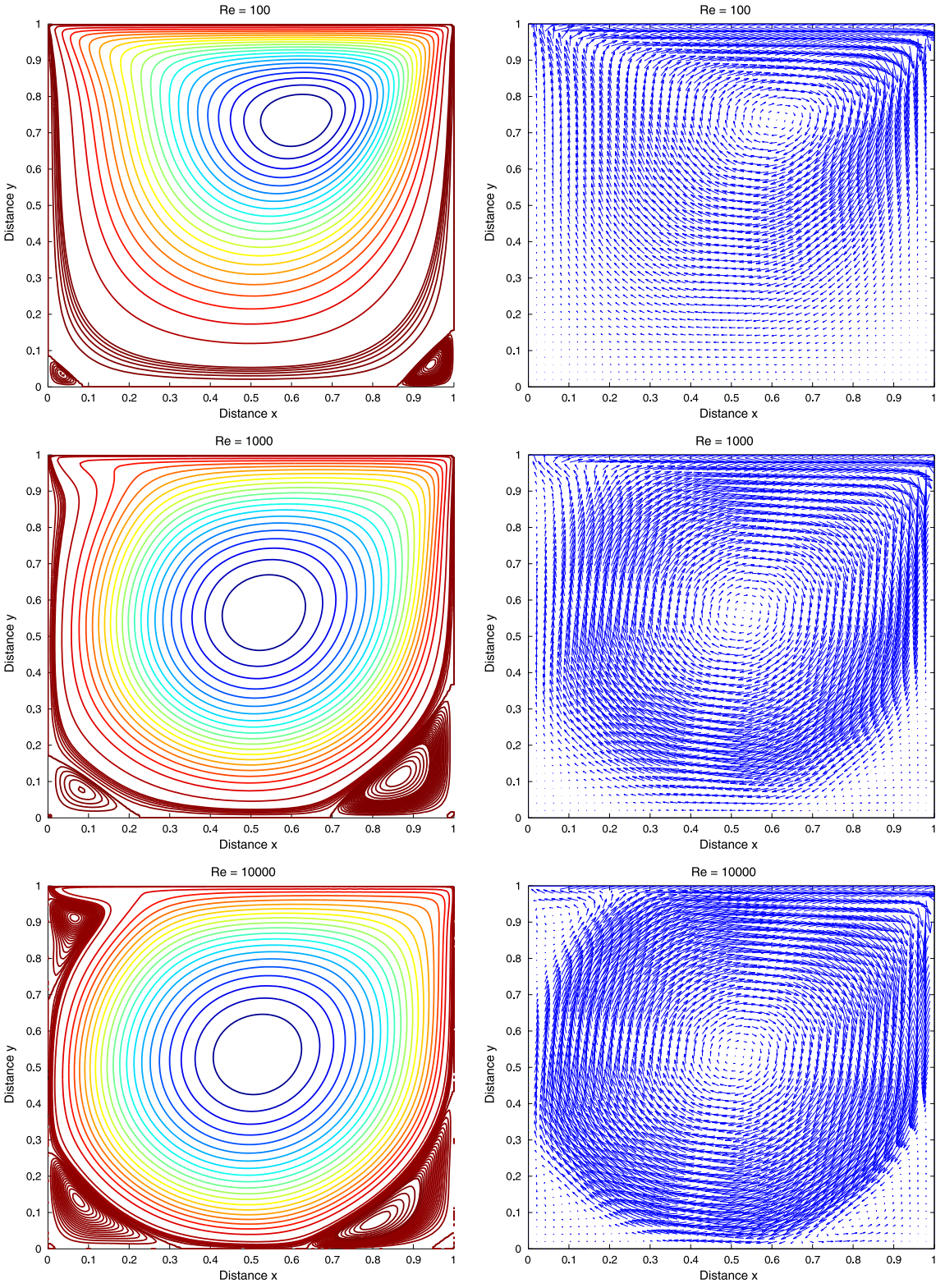

Fig. 11. Stream lines (first column) and velocity fields (second column) for the lid-driven cavity flow.

free and on the other hand free from any Riemann solver or upwind discretization. These properties make the proposed method very attractive since mesh generation and Riemann solvers are not required in its formulation. To examine the accuracy of the meshless method we solve several test problems for linear and nonlinear convection–diffusion flows. Comparison to the well-established semi-Lagrangian method widely used in the literature to solve this kind of applications has been presented in our study. The method is also applied to solve a transport problem in the north sea. The obtained numerical results confirm the accuracy of the proposed meshless method and its performance for this type of flow problems.

Finally, although we have restricted our numerical computations to the case of two dimensional convection-dominated problems using fixed sets of collocation points, the more important implications of our research concern the use of effective stabilized meshless methods for computational fluid dynamic problems in three spatial dimensions implemented in parallel processing and using adaptive sets of collocation points for the radial basis functions.

Acknowledgments

The authors would like to thank anonymous referees for giving very helpful comments and suggestions that have greatly improved this paper. Financial support provided by CNRST through the project FINCOME 2015 is also gratefully acknowledged.

References

[1] S.N. Atluri, T. Zhu, A new meshless local petrov-galerkin (MLPG) approach in computational mechanics, Comput. Mech. 22 (1998) 117–127.
[2] T. Belytschko, Y. Krongauz, D. Organ, M. Fleming, P. Krysl, Meshless methods: An overview and recent developments, Comput. Methods Appl. Mech. Engrg. 139 (1996) 3–47.
[3] F. Benkhaldoun, A. Halassi, D. Ouazar, M. Seaid, A. Taik, Slope limiters for radial basis functions applied to conservation laws with discontinuous flux function, Eng. Anal. Bound. Elem. 66 (2016) 49–65.
[4] F. Benkhaldoun, M. Seaid, A simple finite volume method for the shallow water equations, J. Comput. Appl. Math. 234 (2010) 58–72.
[5] M. Buhamman, Radial Basis Functin: Theory and Implementations, Cambridge University Press, 2003.
[6] M. Buhmann, S. Dinew, E. Larsson, A note on radial basis function interpolant limits, IMA J. Numer. Anal. 30 (2010) 543–554.
[7] Y.L. Chan, L.H. Shen, C.T. Wu, D.L. Young, A novel upwind based local radial basis function differential quadrature method for convection-dominated flows, Comput. & Fluids 89 (2014) 157–166.
[8] C.N. Dawson, Godunov-mixed methods for advective flow problems in one space dimension, SIAM J. Numer. Anal. 28 (1991) 1282–1309.
[9] J. Douglas, T.F. Russell, Numerical methods for convection dominated diffusion problems based on combining the method of characteristics with finite elements or finite differences, SIAM J. Numer. Anal. 19 (1982) 871–885.
[10] M. El-Amrani, M. Seaid, An essentially non-oscillatory semi-Lagrangian method for tidal flow simulations, Internat. J. Numer. Methods Engrg. 81 (2010) 805–834.
[11] R. Franke, Scattered data interpolation: tests of some methods, Math. Comp. 48 (1979) 181–200.
[12] Ghia, K.N. Ghia, C.T. Shin, High-Re solutions for incompressible flow using the Navier-Stokes equations and multigrid method, J. Comput. Phys. 48 (1982) 387–411.
[13] M.A. Golberg, C.S. Chen, The theory of radial basis function applied to the BEM for inhomogeneous partial differential equations, Bound. Elem. Commun. 5 (1994) 57–61.
[14] G. Golub, W. Kahan, Calculating the singular values and pseudo-inverse of a matrix, J. Soc. Ind. Appl. Math. Ser. B: Numer. Anal. 2 (2) (1965) 205–224.
[15] E.J. Kansa, Multiquadrics-a scattered data approximation scheme with applications to computational fluid-dynamics-I surface approximations and partial derivative estimates, Comput. Math. Appl. 19 (1990) 127–145.
[16] E.J. Kansa, H. Power, G.E. Fasshauer, L. Ling, A volumetric integral radial basis function method for time-dependent partial differential equations I. Formulation, Eng. Anal. Bound. Elem. 28 (2004) 1191–1206.
[17] A. Khoshfetrat, M.J. Abedini, Numerical modeling of long waves in shallow water using LrBF-DQ and hybrid DQ/LRBF-DQ, Ocean Modell. 65 (2013) 1–10.
[18] S.V. Krisnamachari, L.J. Hayes, T.F. Russel, A finite element alternating-direction method combined with a modified method of characteristics for convection–diffusion problems, SIAM J. Numer. Anal. 26 (1989) 1462–1473.
[19] C.A. Micchelli, Interpolation of scattered data: Distance matrices and conditionally positive definite functions, Constr. Approx. 2 (1986) 11–22.
[20] K.W. Morton, Numerical Solution of Convection–Diffusion Problems, Chapman & Hall, London, 1996.
[21] M.J.D. Powell, The theory of radial basis function approximation in 1990, in advances in numerical analysis, in: W. Light (Ed.), Wavelets, Subdivision Algoritms and Radial Functions Vol. II, Oxford University Press, UK, 1992, pp. 105–210.
[22] A. Robert, A stable numerical integration scheme for the primitive meteorological equations, Atmos. Ocean 22 (1984) 283–308.
[23] Y.V.S.S. Sanyasiraju, G. Chandhini, Local radial basis function based gridfree scheme for unsteady incompressible viscous flows, J. Comput. Phys. 227 (2008) 8922–8948.
[24] S.A. Sarra, A local radial basis function method for advection–diffusion-reaction equations on complexly shaped domains, J. Appl. Math. Comput. 218 (2012) 9853–9865.

[25] A. Shirzadi, Numerical solutions of 3d Cauchy problems of elliptic operators in cylindrical domain using local weak equations and radial basis functions, Int. J. Comput. Math. (2015) 1–11.
[26] A. Shirzadi, V. Sladek, J. Sladek, A local integral equation formulation to solve coupled nonlinear reaction–diffusion equations by using moving least square approximation, Eng. Anal. Bound. Elem. 37 (1) (2013) 8–14.
[27] C. Shu, An upwind local rbf-dq method for simulation of inviscid compressible flows, Comput. Methods Appl. Mech. Eng. 194 (2005) 2001–2017.
[28] C. Shu, S. Osher, Efficient implementation of essentially non-oscillatory shock capturing schemes, J. Comput. Phys. 77 (1988) 439–471.
[29] A. Staniforth, J. Côté, Semi-lagrangian integration schemes for the atmospheric models: A review, Weather Rev. 119 (1991) 2206–2223.
[30] F. Takhtabnoos, A. Shirzadi, A new implementation of the finite collocation method for time dependent {PDEs}, Eng. Anal. Bound. Elem. 63 (2016) 114–124.
[31] H. Wendland, Scattered Data Approximation, Cambridge University Press, 2005.
[32] S.M. Wong, Y.C. Hon, M.A. Golberg, Compactly supported radial basis functions shallow water equations, J. Appl. Sci. Comput. 127 (2002) 79–101.